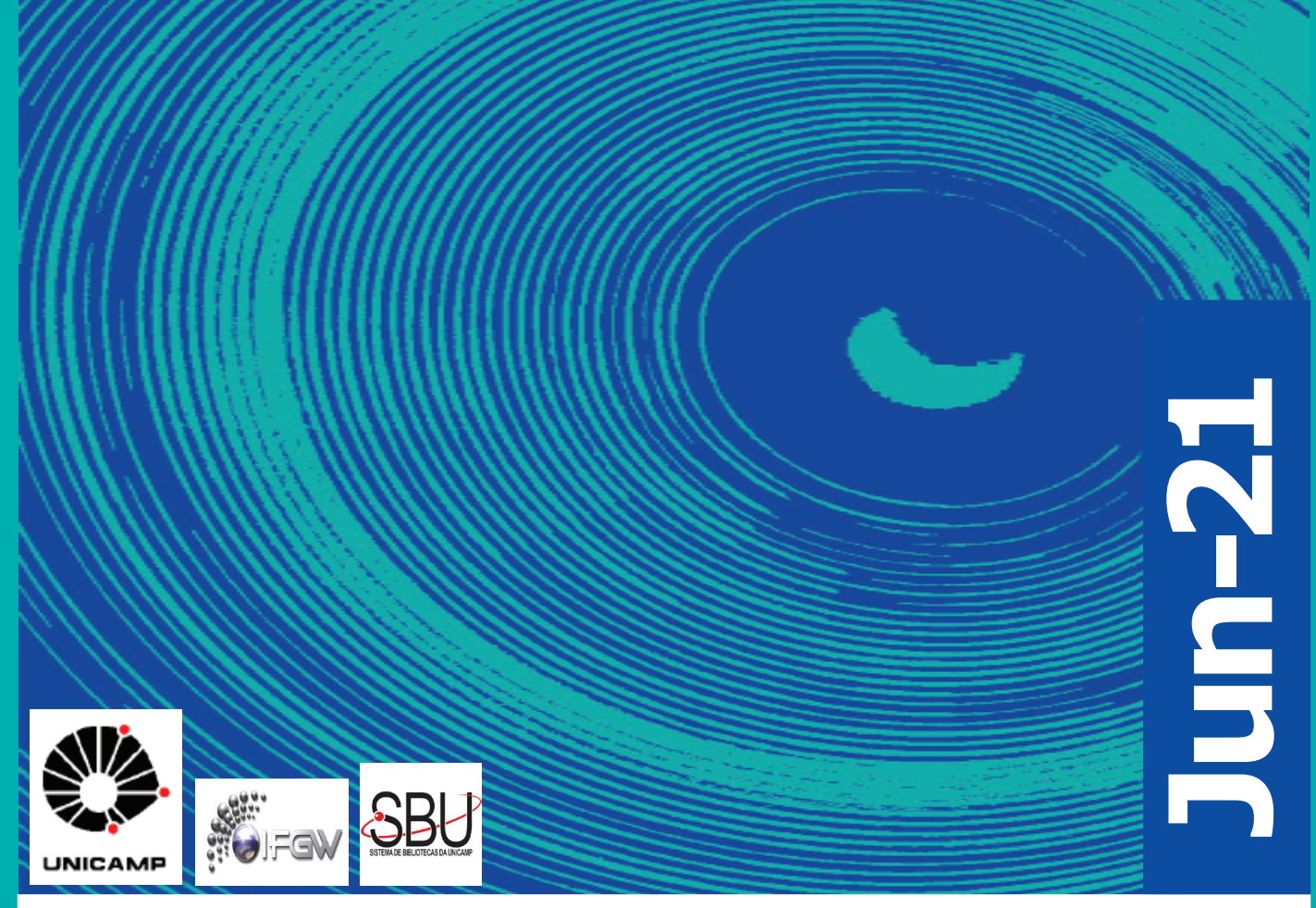
## Abstracta

Ano XXV - N. 03



Artigos publicados P078-2021 à P122-2021

Correções Co006-2021

Defesas de Dissertações do IFGW D009-2021 à D011-2021

Defesas de Teses do IFGW T004-2021 à T007-2021

## **Artigos publicados**

[P078-2021] "A new phenomenological model for annealing of fission tracks in apatite: laboratory data fitting and geological benchmarking"

Rana, M. A.; Lixandrao Filho, A. L.\*; Guedes, S.\*

Rana track annealing model 2007, based on an Arrhenius approach, is significantly modified, including new assumptions, fitting parameters, and analysis, to yield a new phenomenological model for annealing of fission tracks in apatite. Construction and optimization of the new six parameter model have been described in detail. The model shows a hybrid behavior. In Arrhenius plot, for higher temperatures (laboratory data included), iso--annealing lines are curved while, for low temperatures (geological time scale), iso-annealing lines become parallel straight lines. This is a new feature for any such model and has produced promising results. C-axis projected lengths from laboratory experiments on Durango apatite are employed to find model parameters. KTB borehole fission-track data are added to build the temperature function that modifies the original equation. Partial annealing zone (PAZ), closure temperature (T-C) and total annealing temperature (T-A) were calculated and compared to geological benchmarks. The predictions of the present model agreed well with low and high temperature benchmarks. PAZ, T-C and T-A predictions were also compared to the Fanning Curvilinear Arrhenius model predictions, resulting in good agreement. The present model is flexible enough to be applied to other fission- track systems, like zircon, muscovite and titanite.

PHYSICS AND CHEMISTRY OF MINERALS 48[5], 21, 2021. DOI: 10.1007/s00269-021-01143-9

[P079-2021] "A reactive molecular dynamics study on the mechanical properties of a recently synthesized amorphous carbon monolayer converted into a nanotube/nanoscroll"

Pereira Junior, M. L.; Cunha, W. F. da; Galvao, D. S.\*; Ribeiro Junior, L. A.

Recently, laser-assisted chemical vapor deposition has been used to synthesize a free-standing, continuous, and stable monolayer amorphous carbon (MAC). MAC is a pure carbon structure composed of randomly distributed five, six, seven, and eight atom rings, which is different from that of disordered graphene. More recently, amorphous MAC-based nanotubes (a-CNT) and nanoscrolls (a-CNS) were proposed. In this work, we have investigated (through fully atomistic reactive molecular dynamics simulations) the mechanical properties and sublimation points of pristine and a-CNT and a-CNS. The results showed that a-CNT and a-CNS have distinct elastic properties and fracture patterns compared to those of their pristine analogs. Both a-CNT and a-CNS presented a non-elastic regime before their total rupture, whereas the CNT and CNS underwent a direct conversion to fractured forms after a critical strain threshold. The critical strain values for the fracture of the a-CNT and a-CNS are about 30% and 25%, respectively, and they are lower than those of the corresponding CNT and CNS cases. Although less resilient to tension, the amorphous tubular structures have similar thermal stability in relation to the pristine cases with sublimation points of 5500 K, 6300 K, 5100 K, and 5900 K for a-CNT, CNT, a-CNS, and CNS, respectively. An interesting result is that the nanostructure behavior is substantially different depending on whether it is a nanotube or a nanoscroll, thus indicating that the topology plays an important role in defining its elastic properties.

PHYSICAL CHEMISTRY CHEMICAL PHYSICS 23[15] 9089-9095, 2021. DOI: 10.1039/d0cp06613c

[P080-2021] "Angular analysis of the decay B+-> K\*(892)(+) mu(+)mu(-) in proton-proton collisions at root s=8 TeV"

Sirunyan, A. M.; Tumasyan, A.; Adam, W.; Chinellato, J. A.\*; Tonelli Manganote, E. J.\*; et al.; CMS Collaboration

Angular distributions of the decay B+->  $K^*(892)(+)$ mu(+)mu(-) are studied using events collected with the CMS detector in root s = 8 TeV proton-proton collisions at the LHC, corresponding to an integrated luminosity of 20.0 fb(-1). The forward-backward asymmetry of the muons and the longitudinal polarization of the  $K^*(892)(+)$  meson are determined as a function of the square of the dimuon invariant mass. These are the first results from this exclusive decay mode and are in agreement with a standard model prediction.

JOURNAL OF HIGH ENERGY PHYSICS 4, 124, 2021. DOI: 10.1007/JHEP04(2021)124

[P081-2021] "Atomically Precise Bottom-Up Synthesis of h-BNC: Graphene Doped with h-BN Nanoclusters"

Herrera-Reinoza, N.\*; Santos, A. C. dos\*; Lima, L. H. de; Landers, R.\*; Siervo, A. de\*

Monolayer hexagonal boron-nitrogen-carbon (h-BNC) is considered a prominent candidate for the next generation of semiconductor electronic devices. Nevertheless, experimental evidence of h-BNC formation is limited, including a detailed study of its morphological and electronic properties. Here, successful growth of h-BNC from an unexplored single molecular precursor (hexamethyl borazine, C6H18B3N3) using a conventional CVD approach on Ir(111) is reported. The conformation structure of the monolayer and its correlation with the local electronic properties are discussed based on scanning tunneling microscopy/ spectroscopy (STM/STS) and X-ray photoelectron spectroscopy (XPS) results. The results show an h-BNC structure that can be described as BN-doped graphene since the moire 'lattice parameter is preserved along with the alloy. This BN-doped cluster, renamed as h-BN "nanodonuts" according to the electronic density exhibited in STM images, have a tendency to place specific positions within the moire superstructure, and it is constituted by at least (BN)(8) units arranged in a 6-fold BN rings conformation, as evidenced by simulation of STM images based on density functional theory (DFT). For a BN concentration of about 17%, a band gap between 1.4 and 1.6 eV was determined. The versatility of the novel molecular precursor is proven by the growth of a high-quality h-BN monolayer on Rh(111).

CHEMISTRY OF MATERIALS 33[8], 2871-2882, 2021. DOI: 10.1021/acs.chemmater.1c00081 (Artigo destaque de capa)

[P082-2021] "Blood flow response to orthostatic challenge identifies signatures of the failure of static cerebral autoregulation in patients with cerebrovascular disease"

Gregori-Pla, C.; Mesquita, R. C.\*; Favilla, C. G.; Busch, D. R.; Blanco, I.; Zirak, P.; Frisk, L. K.; Avtzi, S.; Maruccia, F.; Giacalone, G.; Cotta, G.; Camps-Renom, P.; Mullen, M. T.; Marti-Fabregas, J.; Prats-Sanchez, L.; Martinez-Domeno, A.; Kasner, S. E.; Greenberg, J. H.; Zhou, C.; Edlow, B. L.; Putt, M. E.; Detre, J. A.; Yodh, A. G.; Durduran, T.; Delgado-Mederos, R.

Background The cortical microvascular cerebral blood flow response (CBF) to different changes in head-of-bed (HOB) position has been shown to be altered in acute ischemic stroke (AIS) by diffuse correlation spectroscopy (DCS) technique. However, the relationship between these relative Delta CBF changes and associated systemic blood pressure changes has not been studied, even though blood pressure is a major driver of cerebral blood flow.

Methods Transcranial DCS data from four studies measuring bilateral frontal microvascular cerebral blood flow in healthy controls (n = 15), patients with asymptomatic severe internal carotid artery stenosis (ICA, n = 27), and patients with acute ischemic stroke (AIS, n = 72) were aggregated. DCS-measured CBF was measured in response to a short head-of-bed (HOB) position manipulation protocol (supine/elevated/supine, 5 min at each position). In a sub-group (AIS, n = 26; ICA, n = 14; control, n = 15), mean arterial pressure (MAP) was measured dynamically during the protocol. Results After elevated positioning, DCS CBF returned to baseline supine values in controls (p = 0.890) but not in patients with AIS (9.6% [6.0,13.3]), mean 95% CI, p < 0.001) or ICA stenosis (8.6% [3.1,14.0], p = 0.003)). MAP in AIS patients did not return to baseline values (2.6 mmHg [0.5, 4.7], p = 0.018), but in ICA stenosis patients and controls did. Instead ipsilesional but not contralesional CBF was correlated with MAP (AIS 6.0%/mmHg [- 2.4,14.3], p = 0.038; ICA stenosis 11.0%/mmHg [2.4,19.5], p < 0.001). Conclusions The observed associations between ipsilateral CBF and MAP suggest that short HOB position changes may elicit deficits in cerebral autoregulation in cerebrovascular disorders. Additional research is required to further characterize this phenomenon.

**BMC NEUROLOGY 21[1], 154, 2021. DOI:** 10.1186/s12883-021-02179-8

[P083-2021] "Calibration of the underground muon detector of the Pierre Auger Observatory"

Aab, A.; Abreu, P.; Aglietta, M.; Chinellato, J. A.\*; Franco, D. de Oliveira\*; Dobrigkeit, C.\*; Fauth, A. C.\*; Payeras, A. Machado\*; Muller, M. A.\*; et al.; Pierre Auger Collaboration

To obtain direct measurements of the muon content of extensive air showers with energy above 10(16.5) eV, the Pierre Auger Observatory is currently being equipped with an underground muon detector (UMD), consisting of 219 10m(2)-modules, each segmented into 64 scintillators coupled to silicon photomultipliers (SiPMs). Direct access to the shower muon content allows for the study of both of the composition of primary cosmic rays and of high-energy hadronic interactions in the forward direction. As the muon density can vary between tens of muons per m(2) close to the intersection of the shower axis with the ground to much less than one per m(2) when far away, the necessary broad dynamic range is achieved by the simultaneous implementation of two acquisition modes in the read-out electronics: the binary mode, tuned to count single muons, and the ADC mode, suited to measure a high number of them. In this work, we present the end-to-end calibration of the muon detector modules: first, the SiPMs are calibrated by means of the binary channel, and then, the ADC channel is calibrated using atmospheric muons, detected in parallel to the shower data acquisition. The laboratory and field measurements performed to develop the implementation of the full calibration chain of both binary and ADC channels are presented and discussed. The calibration procedure is reliable to work with the high amount of channels in the UMD, which will be operated continuously, in changing environmental conditions, for several years.

JOURNAL OF INSTRUMENTATION 16[4], P04003, 2021. DOI: 10.1088/1748-0221/16/04/P04003

[P084-2021] "Crystal, local atomic, and local electronic structures of YbFe2Zn20-xCdx (0 <= x <= 1.4): A multiband system with possible coexistence of light and heavy fermions"

Fahl, A\*; Grossi, R.\*; Rigitano, D.\*; Cabrera-Baez, M.; Avila, M. A.; Adriano, C.\*; Granado, E.\*

The partial (up to 7%) substitution of Cd for Zn in the Yb-based heavy-fermion material YbFe2Zn20 is known to induce a slight (similar to 20%) reduction of the Sommerfeld specific-heat coefficient gamma and a huge (up to two orders of magnitude) reduction of the T-2 resistivity coefficient A, corresponding to a drastic and unexpected reduction of the Kadowaki-Woods ratio A/gamma(2). Here, Yb L-3-edge x-ray absorption spectroscopy shows that the Yb valence state is close to 3+ for all x, whereas x-ray diffraction reveals that Cd replaces the Zn ions only at the 16c site of the Fd (3) over barm cubic structure, leaving the 48f and 96g sites with full Zn occupation. Ab initio electronic structure calculations in pure and Cd-doped materials, carried out without considering correlations, show multiple conduction bands with only minor modifications of the band dispersions near the Fermi level and therefore do not explain the resistivity drop introduced by Cd substitution. We propose that the site-selective Cd substitution introduces light conduction bands with a substantial contribution of Cd(16c) 5p levels that have weak coupling to the Yb3+ 4f moments. These light fermions coexist with heavy fermions that originate from other conduction bands with larger participation of Zn(96g) 4p levels that remain strongly coupled with the Yb3+ local moments.

PHYSICAL REVIEW B 103[15], 155116, 2021. DOI: 10.1103/ PhysRevB.103.155116

[P085-2021] "Development and validation of HERWIG 7 tunes from CMS underlying-event measurements"

Sirunyan, A. M.; Tumasyan, A.; Adam, W.; Chinellato, J. A.\*; Tonelli Manganote, E. J.\*; et al.; CMS Collaboration

This paper presents new sets of parameters ("tunes") for the underlying-event model of the herwig 7 event generator. These parameters control the description of multiple-parton interactions (MPI) and colour reconnection in herwig 7, and are obtained from a fit to minimum-bias data collected by the CMS experiment at v = 0.9, 7, and 13 TeV. The tunes are based on the NNPDF3.1 next-to-nextto-leading-order parton distribution function (PDF) set for the parton shower, and either a leading--order or next-to-nextto-leading-order PDF set for the simulation of MPI and the beam remnants. Predictions utilizing the tunes are produced for event shape observables in electron-positron collisions, and forminimum-bias, inclusive jet, top quark pair, and Zand Wboson events in proton-proton collisions, and are compared with data. Each of the new tunes describes the data at a reasonable level, and the tunes using a leading-order PDF for the simulation of MPI provide the best description of the data.

**EUROPEAN PHYSICAL JOURNAL C 81[4], 312, 2021. DOI:** 10.1140/epjc/s10052-021-08949-5

[P086-2021] "Enantioselection and chiral sorting of single microspheres using optical pulling forces"

Ali, R.\*; Dutra, R. S.; Pinheiro, F. A.; Neto, P. A. Maia

We put forward a novel, twofold scheme that enables, at the same time, all-optical enantioselection and sorting of single multipolar chiral microspheres based on optical pulling forces exerted by two non-collinear, non-structured, circularly polarized light sources. Our chiral resolution method can be externally controlled by varying the angle between their incident wavevectors, allowing for fine-tuning of the range of chiral indices for enantioselection. Enantioselectivity is achieved by choosing angles such that only particles with the same handedness of the light sources are pulled. This proposal allows one to achieve all-optical sorting of chiral microspheres with arbitrarily small chiral parameters, thus outperforming current optical methods.

**OPTICS LETTERS 46[7], 1640-1643, 2021. DOI:** 10.1364/OL.419150

[P087-2021] "Engineering Shape Anisotropy of Fe3O4-gamma-Fe2O3 Hollow Nanoparticles for Magnetic Hyperthermia"

Niraula, G.; Coaquira, J. A. H.; Zoppellaro, G.; Villar, B. M. G.; Garcia, F.; Bakuzis, A. F.; Longo, J. P. F.; Rodrigues, M. C.; Muraca, D.\*; Ayesh, A. I.; Sinfronio, F. S. M.; Menezes, A. S. de; Goya, G. F.; Sharma, S. K.

The use of microwave-assisted synthesis (in water) of alpha--Fe2O3 nanomaterials followed by their transformation onto iron oxide Fe3O4-gamma-Fe2O3 hollow nanoparticles encoding well-defined sizes and shapes [nanorings (NRs) and nanotubes (NTs)] is henceforth described. The impact of experimental variables such as concentration of reactants, volume of solvent employed, and reaction times/temperatures during the shape-controlled synthesis revealed that the key factor that gated generation of morphologically diverse nanoparticles was associated to the initial concentration of phosphate anions employed in the reactant mixture. All the nanomaterials presented were fully characterized by powder X-ray diffraction, field emission scanning electron microscopy, Fourier transform infrared, Mossbauer spectroscopy, and superconducting quantum interference device (SQUID). The hollow nanoparticles that expressed the most promising magnetic responses, NTs and NRs, were further tested in terms of efficiencies in controlling the magnetic hyperthermia, in view of their possible use for biomedical applications, supported by their excellent viability as screened by in vitro cytotoxicity tests. These systems NTs and NRs expressed very good magneto-hyperthermia properties, results that were further validated by micromagnetic simulations. The observed specific absorption rate (SAR) and intrinsic loss power of the NRs and NTs peaked the values of 340 W/g and 2.45 nH m(2) kg(-1) (NRs) and 465 W/g and 3.3 nH m(2) kg(-1) (NTS), respectively, at the maximum clinical field 450 Oe and under a frequency of 107 kHz and are the highest values among those reported so far in the hollow iron--oxide family. The higher SAR in NTs accounts the importance of magnetic shape anisotropy, which is well-predicted by the modified dynamic hysteresis (beta-MDH) theoretical model.

ACS APPLIED NANO MATERIALS 4[3], 3148-3158, 2021. DOI: 10.1021/acsanm.1c00311

[P088-2021] "First measurement of quarkonium polarization in nuclear collisions at the LHC"

Acharya, S.; Adamova, D.; Adler, A.; Albuquerque, D. S. D.\*; Chinellato, D. D.\*; Takahashi, J.\*; et al.; ALICE Collaboration

The polarization of inclusive J/psi and Upsilon(1S) produced in Pb-Pb collisions at root s(NN) = 5.02 TeV at the LHC is measured with the ALICE detector. The study is carried out by reconstructing the quarkonium through its decay to muon pairs in the rapidity region 2.5 < y < 4 and measuring the polar and azimuthal angular distributions of the muons. The polarization parameters lambda(theta), lambda(phi) and lambda(theta phi) are measured in the helicity and Collins--Soper reference frames, in the transverse momentum interval 2 < p(T) < 10 GeV/c and p(T) < 15 GeV/c for the J/psi and Upsilon(1S), respectively. The polarization parameters for the J/psi are found to be compatible with zero, within a maximum of about two standard deviations at low p(T), for both reference frames and over the whole p(T) range. The values are compared with the corresponding results obtained for pp collisions at root s = 7 and 8 TeV in a similar kinematic region by the ALICE and LHCb experiments. Although with much larger uncertainties, the polarization parameters for Upsilon(1S) production in Pb-Pb collisions are also consistent with zero.

**PHYSICS LETTERS B 815, 136146, 2021. DOI:** 10.1016/j.physletb.2021.136146

[P089-2021] "Functionalized microchannels as xylem-mimicking environment: Quantifying X. fastidiosa cell adhesion"

Monteiro, M. P.\*; Hernandez-Montelongo, J.\*; Sahoo, P. K.\*; Montelongo, R. H.; Oliveira, D. S. de; Piazzeta, M. H. O.; Garcia Sandoval, J. P.; Souza, A. A. de; Gobbi, A. L.; Cotta, M. A.\*

Microchannels can be used to simulate xylem vessels and investigate phytopathogen colonization under controlled conditions. In this work, we explore surface functionalization strategies for polydimethylsiloxane and glass microchannels to study microenvironment colonization by Xylella fastidiosa subsp. pauca cells. We closely monitored cell initial adhesion, growth, and motility inside microfluidic channels as a function of chemical environments that mimic those found in xylem vessels. Carboxymethylcellulose (CMC), a synthetic cellulose, and an adhesin that is overexpressed during early stages of X. fastidiosa biofilm formation, XadA1 protein, were immobilized on the device's internal surfaces. This latter protocol increased bacterial density as compared with CMC. We quantitatively evaluated the different X. fastidiosa attachment affinities to each type of microchannel surface using a mathematical model and experimental observations acquired under constant flow of culture medium. We thus estimate that bacterial cells present similar to 4 and 82% better adhesion rates in CMC- and XadA1-functionalized channels, respectively. Furthermore, variable flow experiments show that bacterial adhesion forces against shear stresses approximately doubled in value for the XadA1-functionalized microchannel as compared with the polydimethylsiloxane and glass pristine channels. These results show the viability of functionalized microchannels to mimic xylem vessels and corroborate the important role of chemical environments, and particularly XadA1 adhesin, for early stages of X. fastidiosa biofilm formation, as well as adhesivity modulation along the pathogen life cycle.

BIOPHYSICAL JOURNAL 120[8], 1443-1453, 2021. DOI: 10.1016/j.bpj.2021.02.009

[P090-2021] "Hollow Core Inhibited Coupled Antiresonant Terahertz Fiber: A Numerical and Experimental Study"

Sultana, J.; Islam, M. S.; Cordeiro, C. M. B.\*; Habib, M. S.; Dinovitser, A.; Kaushik, M.; Ng, B. W. H.; Heidepriem, H. E.; Abbott, D.

In this article, a hollow core antiresonant photonic crystal fiber is analyzed for terahertz applications. A numerical analysis of the proposed fiber is first carried out to minimize coupling between the core and cladding modes. The modeling of the scaled-up and inhibited coupling fiber is carried out by means of a finite element method, which is then demonstrated using a Zeonex filament fiber, fabricated by fused deposition modeling of 3-D printing technology. The simulation is carried out to analyze both the transmission and possibility of refractometric sensing, whereas the experimental analysis is carried out using terahertz time-domain spectroscopy, and supports our numerical findings, illustrating how the proposed fibers can be used for low-loss transmission of terahertz waves. The simplicity of the proposed fiber structures facilitates fabrication for a number of different transmission and sensing applications in the terahertz range.

IEEE TRANSACTIONS ON TERAHERTZ SCIENCE AND TECHNOLO-GY 11[3], 245-260, 2021. DOI: 10.1109/TTHZ.2020.3031727

[P091-2021] "How Crystallization Affects the Oriented Attachment of Silver Nanocrystals"

Faccin, G. M.\*; Pereira, Z. S.; Silva, E. Z.\* da

Oriented attachment processes between nanocrystals provide a promising route for the synthesis of mesocrystals that, although made of the same elements as their usual crystal counterparts, nevertheless possess very distinct physical and chemical properties that can be explored for technological applications. In this study, the oriented attachment process experimentally observed between silver nanocrystals is analyzed through a systematic approach involving a series of molecular dynamics simulations. The simulations elucidate how the crystallization process between silver nanocrystals leads to either imperfect oriented attachment or perfect oriented attachment, how likely those processes are to occur and how faceting affects their outcome. This information can be explored to develop new strategies aimed at triggering specific crystallization processes that take place during mesocrystal growth, thus allowing control over the characteristics of the final synthesized material.

JOURNAL OF PHYSICAL CHEMISTRY C 125[12], 6812-6820, 2021. DOI: 10.1021/acs.jpcc.0c10321

[P092-2021] "Intermodal Brillouin scattering in solid-core photonic crystal fibers"

Jarschel, P. F.\*; Lamilla, E.\*; Espinel, Y. A. V.\*; Aldaya, I.\*; Pita, J. L.\*; Gil-Molina, A.\*; Wiederhecker, G. S.\*; Dainese, P.\*

We investigate intermodal forward Brillouin scattering in a solid-core photonic crystal fiber (PCF), demonstrating efficient power conversion between the HE11 and HE21 modes, with a maximum gain coefficient of 21.4 W-1 km(-1). By exploring mechanical modes of different symmetries, we observe both polarization-dependent and polarization-independent intermodal Brillouin interaction. Finally, we discuss the role of squeeze film air damping and leakage mechanisms, ultimately critical to the engineering of PCF structures with enhanced interaction between high-order optical modes through flexural mechanical modes.

APL PHOTONICS 6[3], 036108, 2021. DOI: 10.1063/5.0040580

[P093-2021] "Invisible neutrino decay: first vs second oscillation maximum"

Chakraborty, K.; Dutta, D.; Goswami, S.; Pramanik, D.\*

We study the physics potential of the long-baseline experiments T2HK, T2HKK and ESS nu SB in the context of invisible neutrino decay. We consider normal mass ordering and assume the state nu (3) as unstable, decaying into sterile states during the flight and obtain constraints on the neutrino decay lifetime (tau (3)). We find that T2HK, T2HKK and ESS nu SB are sensitive to the decay-rate of nu (3) for tau (3)/m(3)  $= 2.72 \times 10(-11)$ s/eV, tau (3)/m(3)  $= 4.36 \times 10(-11)$ s/eV and  $tau (3)/m(3) \le 2.43 \times 10(-11)s/eV$  respectively at 3 sigma C.L. We compare and contrast the sensitivities of the three experiments and specially investigate the role played by the mixing angle theta (23). It is seen that for experiments with flux peak near the second oscillation maxima, the poorer sensitivity to theta (23) results in weaker constraints on the decay lifetime. Although, T2HKK has one detector close to the second oscillation maxima, having another detector at the first oscillation maxima results in superior sensitivity to decay. In addition, we find a synergy between the two baselines of the T2HKK experiment which helps in giving a better sensitivity to decay for theta (23) in the higher octant. We discuss the octant sensitivity in presence of decay and show that there is an enhancement in sensitivity which occurs due to the contribution from the survival probability P-mu mu is more pronounced for the experiments at the second oscillation maxima. We also obtain the combined sensitivity of T2HK+ESS nu SB and T2HKK+ESS nu SB as tau  $(3)/m(3) \le 4.36 \times 10(-11)$ s/eV and tau  $(3)/m(3) \le 5.53 \times 10(-11)$ s/eV respectively at 3 sigma C.L.

JOURNAL OF HIGH ENERGY PHYSICS 5, 91, 2021. DOI: 10.1007/JHEP05(2021)091

[P094-2021] "Jarzynski Equality for Conditional Stochastic Work"

Sone, A.; Deffner, S.\*

It has been established that the inclusive work for classical, Hamiltonian dynamics is equivalent to the two-time energy measurement paradigm in isolated quantum systems. However, a plethora of other notions of quantum work has emerged, and thus the natural question arises whether any other quantum notion can provide motivation for purely classical considerations. In the present analysis, we propose the conditional stochastic work for classical, Hamiltonian dynamics, which is inspired by the one-time measurement approach. This novel notion is built upon the change of expectation value of the energy conditioned on the initial energy surface. As main results, we obtain a generalized Jarzynski equality and a sharper maximum work theorem, which account for how non-adiabatic the process is. Our findings are illustrated with the parametric harmonic oscillator.

JOURNAL OF STATISTICAL PHYSICS 183[1], 11, 2021. DOI: 10.1007/s10955-021-02720-6

[P095-2021] "Lambda K femtoscopy in Pb-Pb collisions at root s(NN)=2.76 TeV"

Acharya, S.; Adamova, D.; Adler, A.; Albuquerque, D. S. D.\*; Chinellato, D. D.\*; Takahashi, J.\*; et al.; ALICE Collaboration

The first measurements of the scattering parameters of Lambda K pairs in all three charge combinations (Lambda K+, Lambda K-, and Lambda K-S(0)) are presented. The results are achieved through a femtoscopic analysis of Lambda K correlations in Pb-Pb collisions at root s(NN) = 2.76 TeV recorded by ALICE at the Large Hadron Collider. The femtoscopic correlations result from strong final-state interactions and are fit with a parametrization allowing for both the characterization of the pair emission source and the measurement of the scattering parameters for the particle pairs. Extensive studies with the THERMINATOR 2 event generator provide a good description of the nonfemtoscopic background, which results mainly from collective effects, with unprecedented precision. Furthermore, together with HIJING simulations, this model is used to account for contributions from residual correlations induced by feed--down from particle decays. The extracted scattering parameters indicate that the strong force is repulsive in the Lambda K+ interaction and attractive in the Lambda K- interaction. The data hint that the Lambda K-S(0) interaction is attractive; however, the uncertainty of the result does not permit such a decisive conclusion. The results suggest an effect arising either from different quark-antiquark interactions between the pairs (s (s) over bar in Lambda K+ and u (u) over bar in Lambda K-) or from different net strangeness for each system (S = 0 for Lambda K+, and S = -2 for Lambda K-). Finally, the Lambda K systems exhibit source radii larger than expected from extrapolation from identical particle femtoscopic studies. This effect is interpreted as resulting from the separation in space--time of the single-particle Lambda and K source distributions.

PHYSICAL REVIEW C 103[5], 055201, 2021. DOI: 10.1103/ PhysRevC.103.055201 [P096-2021] "Late-time dark matter oscillations and the core-cusp problem"

Cline, J. M.; Gambini, G.\*; McDermott, S. D.; Puel, M.

The core-cusp problem persists as an unresolved tension between the pre- dictions of Lambda CDM cosmology and observations of dark matter (DM) profiles in dwarf spheroidal and other galaxies. We present a novel scenario for converting cusps into cores through reactivation of DM annihilation in galaxies at late times. This can happen in asymmetric DM models when there is a very small DM-number violating mass term that causes oscillations between DM and its antiparticle. Using analytic methods as well as gravitational N-body simulations, we show that this mechanism can robustly eliminate cusps from galactic DM profiles for light fermionic DM of mass m(chi) similar to (0.1 - 1) GeV and a lighter mediator into which the DM can annihilate. We identify regions of parameter space where annihilation of DM particles is more efficient than elastic scattering at reducing the inner density of the DM profile. Dark matter annihilation is therefore a qualitatively distinct alternative to the mechanism of elastic self--interacting dark matter for addressing the cusp-core problem.

JOURNAL OF HIGH ENERGY PHYSICS 4, 223, 2021. DOI: 10.1007/JHEP04(2021)223

[P097-2021] "Lighting of a monochromatic scatterer with virtual gain"

Ali, R.\*

In this work, we discuss the scattering features of a dipolar particle made of large refractive index material by employing the concept of virtual gain and virtual loss. The virtual gain and loss can be achieved in a lossless passive nanostructure by shaping the temporal waveform of incident signals in the complex frequency plane. We show that an appropriate tuning of excitation time of the impinging field allows to capture and release the electromagnetic energy on-demand for an arbitrary time scale in a lossless nanosphere. Thus, the nanosphere obliges to emit monochromatic magnetic light which can be tuned throughout the whole visible spectrum by varying the size of the nanosphere. This proposal may find fruitful applications in lab-on-a-chip technologies and the realization of monochromatic sectoral multipole light source with a large quality factor at nanoscale level.

PHYSICA SCRIPTA 96[9], 095501, 2021. DOI: 10.1088/1402-4896/abf8eb

[P098-2021] "Localization of light induced in ordered colloidal suspensions: powerful sensing tools"

Ermakov, V. A.\*; Martins, W. S.; Wetter, N. U.; Marques, F. C.\*; Jimenez-Villar, E.\*

We study the light-matter coupling by Raman scattering in colloidal suspensions composed by core-shell TiO2@Silica (Rutile@Silica) nanoparticles suspended in ethanol and water solutions. Strong enhancement of the Raman signal per particle is observed as [TiO2@Silica] is increased above a threshold, being stronger in ethanol suspensions. Moreover, above this [TiO2@Silica] threshold, the optical transmittance of the ethanol suspension starts to be considerably lower than in water, despite scattering strength being higher in water. These results are attributed to localization of light induced by strong correlation in the scatterers' position as a consequence of the long-range Coulomb interaction between the TiO2@Silica nanoparticles. Light diffraction in TiO2@Silica suspensions (water and ethanol) shows strong correlation in the scatterers' position (structure seemingly cubic),

being stronger in ethanol than in water (longer-range Coulomb interaction). As a result, we demonstrate in these colloidal suspensions for the first time, to our knowledge, strongly enhanced light-matter coupling through correlation-induced localization with kl(T) much higher than unity and in an ordered colloidal-photonic structure. This strong enhancement of light-matter coupling by localization of light opens an avenue for manufacturing powerful sensing tools.

NANOSCALE 13[13], 6417-6425, 2021. DOI: 10.1039/d0nr08736j

[P099-2021] "Low-temperature electronic transport of manganese silicide shell-protected single crystal nanowires for nanoelectronics applications"

Cruz, A. D. E. da\*; Santos, M. V. P. dos\*; Campanelli, R. B.\*; Pagliuso, P. G.\*; Bettini, J.; Pirota, K. R.\*; Beron, F.\*

Recently, core-shell nanowires have been proposed as potential electrical connectors for nanoelectronics components. A promising candidate is Mn5Si3 nanowires encapsulated in an oxide shell, due to their low reactivity and large flexibility. In this work, we investigate the use of the one-step metallic flux nanonucleation method to easily grow manganese silicide single crystal oxide-protected nanowires by performing their structural and electrical characterization. We find that the fabrication method yields a room-temperature hexagonal crystalline structure with the c-axis along the nanowire. Moreover, the obtained nanowires are metallic at low temperature and low sensitive to a strong external magnetic field. Finally, we observe an unknown electron scattering mechanism for small diameters. In conclusion, the one-step metallic flux nanonucleation method yields intermetallic nanowires suitable for both integration in flexible nanoelectronics as well as low-dimensionality transport experiments.

NANOSCALE ADVANCES, 2021. DOI: 10.1039/d0na00809e

[P100-2021] "Measurement of b jet shapes in proton-proton collisions at root s=5.02 TeV"

Sirunyan, A. M.; Tumasyan, A.; Adam, W.; Chinellato, J. A.\*; Tonelli Manganote, E. J.\*; et al.; CMS Collaboration

We present the first study of charged-hadron production associated with jets originating from b quarks in proton-proton collisions at a center-of-mass energy of 5.02 TeV. The data sample used in this study was collected with the CMS detector at the CERN LHC and corresponds to an integrated luminosity of 27.4 pb(-1). To characterize the jet substructure, the differential jet shapes, defined as the normalized transverse momentum distribution of charged hadrons as a function of angular distance from the jet axis, are measured for b jets. In addition to the jet shapes, the per-jet yields of charged particles associated with b jets are also quantified, again as a function of the angular distance with respect to the jet axis. Extracted jet shape and particle yield distributions for b jets are compared with results for inclusive jets, as well as with the predictions from the pythia and herwig++ event generators.

JOURNAL OF HIGH ENERGY PHYSICS 5, 54, 2021. DOI: 10.1007/JHEP05(2021)054

[P101-2021] "Measurement of differential cross sections for Z bosons produced in association with charm jets in pp collisions at root s=13 TeV"

Sirunyan, A. M.; Tumasyan, A.; Adam, W.; Chinellato, J. A.\*; Tonelli Manganote, E. J.\*; et al.; CMS Collaboration

Measurements are presented of differential cross sections for the production of Z bosons in association with at least one jet initiated by a charm quark in pp collisions at root s = 13TeV. The data recorded by the CMS experiment at the LHC correspond to an integrated luminosity of 35.9 fb(-1). The final states contain a pair of electrons or muons that are the decay products of a Z boson, and a jet consistent with being initiated by a charm quark produced in the hard interaction. Differential cross sections as a function of the transverse momentum p(T)of the Z boson and p(T) of the charm jet are compared with predictions from Monte Carlo event generators. The inclusive production cross section 405.4 +/- 5.6 (stat) +/- 24.3 (exp) +/-3.7 (theo) pb, is measured in a fiducial region requiring both leptons to have pseudorapidity |eta| < 2.4 and p(T)> 10 GeV, at least one lepton with p(T) > 26 GeV, and a mass of the pair in the range 71-111 GeV, while the charm jet is required to have p(T) > 30 GeV and |eta| < 2.4. These are the first measurements of these cross sections in proton-proton collisions at 13 TeV.

JOURNAL OF HIGH ENERGY PHYSICS 4, 109, 2021. DOI: 10.1007/JHEP04(2021)109

[P102-2021] "Measurement of prompt D-0 and D-0 meson azimuthal anisotropy and search for strong electric fields in PbPb collisions at root S-NN=5.02 TeV"

Sirunyan, A. M.; Tumasyan, A.; Adam, W.; Chinellato, J. A.\*; Tonelli Manganote, E. J.\*; et al.; CMS Collaboration

The strong Coulomb field created in ultrarelativistic heavy ion collisions is expected to produce a rapiditydependent difference (Av2) in the second Fourier coefficient of the azimuthal distribution (elliptic flow, v2) between D0 (uc) and D0 (uc) mesons. Motivated by the search for evidence of this field, the CMS detector at the LHC is used to perform the first measurement of Av2. The rapidity-averaged value is found to be (Av2) = 0.001 ? 0.001 (stat)? 0.003 (syst) in PbPb collisions at ?sNN = 5.02 TeV. In addition, the influence of the collision geometry is explored by measuring the D0 and D0mesons v2 and triangular flow coefficient (v3) as functions of rapidity, transverse momentum (pT), and event centrality (a measure of the overlap of the two Pb nuclei). A clear centrality dependence of prompt D0 meson v2 values is observed, while the v3 is largely independent of centrality. These trends are consistent with expectations of flow driven by the initial-state geometry.

PHYSICS LETTERS B 816, 136253, 2021. DOI: 10.1016/j.physletb.2021.136253

[P103-2021] "Measurement of the CP-violating phase phi(s) in the B-s(0) -> J/psi phi(1020) -> mu(+)mu-K+K- channel in proton-proton collisions at root s=13 TeV"

Sirunyan, A. M.; Tumasyan, A.; Adam, W.; Chinellato, J. A.\*; Tonelli Manganote, E. J.\*; et al.; CMS Collaboration

The CP-violating weak phase ?s and the decay width difference ??s between the light and heavy B0s mass eigenstates are measured with the CMS detector at the LHC in a sample of 48 500 reconstructed B0s? J/I) d (1020) ?11+11? K+K? events. The measurement is based on a data sample corresponding to an integrated luminosity of 96.4 fb?1, collected in proton-proton collisions at ?s = 13 TeV in 2017?2018. To extract the values of ?s and ??s, a time-dependent and flavor-tagged angular analysis of the 11+11?K+K? final state is performed. The analysis employs a dedicated tagging trigger and a novel opposite-side muon flavor tagger based on machine learning techniques.

The measurement yields ?s = ?11 ?50 (stat) ? 10 (syst) mrad and ??s = 0.114 ? 0.014 (stat)? 0.007 (syst) ps?1, in agreement with the standard model predictions. When combined with the previous CMS measurement at ?s = 8 TeV, the following values are obtained: ?s = ?21 ? 44 (stat) ? 10 (syst) mrad, ??s = 0.1032 ? 0.0095 (stat) ? 0.0048 (syst) ps?1, a significant improvement over the 8 TeV result.

**PHYSICS LETTERS B 816, 136188, 2021. DOI:** 10.1016/j.physletb.2021.136188

[P104-2021] "On the adsorption mechanism of caffeine on MAPbI(3) perovskite surfaces: a combined UMC-DFT study"

Ribeiro Junior, L. A.; Tromer, R. M.\*; Santos, R. M. dos; Galvao, D. S.\*

Recently, it was experimentally shown that the performance and thermal stability of the perovskite MAPbI(3) were improved upon the adsorption of a molecular layer of caffeine. In this work, we used a hybrid methodology that combines uncoupled monte carlo (UMC) and density functional theory (DFT) simulations to carry out a detailed and comprehensive study of the adsorption mechanism of a caffeine molecule on the surface of MAPbI(3). Our results showed that the adsorption distance and energy of a caffeine molecule on the MAPbI(3) surface are 2.0 angstrom and -0.3 eV, respectively. The caffeine/MAPbI(3) complex presents a direct bandgap of 2.38 eV with two flat intragap bands distanced 1.15 and 2.18 eV from the top of valence bands. Although the energy band levels are not significantly shifted by the presence of caffeine, the interaction MAPbI(3)/perovskite is enough to affect the bands' dispersion, particularly the conduction bands.

PHYSICAL CHEMISTRY CHEMICAL PHYSICS 23[18], 10807-10813, 2021. DOI: 10.1039/d0cp04308g

[P105-2021] "Optoelectronic properties of amorphous carbon-based nanotube and nanoscroll"

Tromer, R. M.\*; Felix, L. C.\*; Ribeiro, L. A.; Galvao, D. S.\*

Free-standing monolayer amorphous carbon (MAC) is a pure carbon structure composed of randomly distributed atom rings with different sizes, which was recently synthesized. In this work, we carried out ab initio and tight-binding calculations to investigate the optoelectronic properties of MAC and its derived nanotube and nanoscroll configurations. Our results show MAC, tube, and scrolls exhibit similar electronic behavior. All structures absorb from infrared to ultraviolet, with maximum absorption peaks the visible-ultra violet (similar to 3.2 eV). The maximum and minimum reflectivity values are in the range 0.3-0.5 (infrared) and 0.1-0.0 (ultraviolet), making these materials good candidates to ultraviolet filters.

PHYSICA E-LOW-DIMENSIONAL SYSTEMS & NANOSTRUCTURES 130, 114683. 2021. DOI: 10.1016/j.physe.2021.114683

[P106-2021] "Oxygen plasma-enhanced covalent biomolecule immobilization on SU-8 thin films: A stable and homogenous surface biofunctionalization strategy"

Anbumani, S.\*; Silva, A. M.\*; Roggero, U. F. S.; Silva, A. M. P. A.; Hernandez-Figueroa, H. E.; Cotta, M. A.\*

SU-8 is an attractive platform for the development of smart biochips owing to its high aspect ratio of micro/ nanostructures fabrication and remarkable optical and biocompatible properties.

However, few works have explored sub-micron SU-8 thin films for applications in new generations of portable bioanalytical devices. In this work we discuss surface properties for the efficient immobilization of different bioanalytical components on SU-8 thin film surfaces. Short exposure time oxygen plasma treatment improved hydrophilicity and activation of surface carboxyl groups of 300 nm-thick SU-8 films, while maintaining surface roughness below 2 nm. Under these optimized surfaces conditions, covalent immobilization of Interleukin-6 and Prostate Specific Antigen antibodies on SU-8 surfaces was evaluated using quantitative fluorescence microscopy. The addition of standard crosslinker, 1-ethyl-3-(3-(dimethylamino)-propyl)--carbodiimide and N-hydroxysuccinimide mixture to our protocol yielded 15?20% higher antibody immobilization due to activation of surface carboxyl groups. The stability of the plasma treatment along time, and the ideal surface passivation of functionalized samples are demonstrated, along with the selective immobilization antibody to photolithographically--patterned SU-8 microstructures. Overall, our optimized protocol could find broad applications of functionalized SU-8 thin films in biomedical fields, particularly for the fabrication of SU-8 based miniaturized photonic and plasmonic biosensors.

**APPLIED SURFACE SCIENCE 553, 149502, 2021. DOI:** 10.1016/j. apsusc.2021.149502

[P107-2021] "Predicted Superconductivity in the Electride Li5C"

Pereira, Z. S.; Faccin, G. M.\*; Silva, E. Z. da\*

Superconductivity under pressure is a very important research path for finding new superconductors, and electrides have been shown to present superconductivity under pressure. In the present work, using density functional theory (DFT) in association with the particle swarm search method (PSO), we discovered a remarkable electride superconductor Li5C with P6/mmm symmetry. This newly predicted material has stability in the range from 50 to 210 GPa, confirmed by phonon analysis and ab initio molecular dynamics. This electride has a two-dimensional (2D) hexagonal anionic electron topology, creating connected electronic channels in the interstitial sites of the crystal. We also show that Li5C has a significant conventional electron-phonon coupling with superconducting critical temperatures (T-c) estimated up to 48.3 K at 210 GPa, which is the highest T-c value already reported for lithium-carbon compounds and one of the highest known transition temperatures predicted for electrides. Even at moderate pressure (50 GPa), this material shows a relatively high T-c value (14.2 K).

JOURNAL OF PHYSICAL CHEMISTRY C 125[16], 8899-8906, 2021. DOI: 10.1021/acs.jpcc.1c02329 (Artigo destaque de capa)

[P108-2021] "Properties of DBD Plasma Jets Using Powered Electrode With and Without Contact With the Plasma"

Nascimento, F. do; Kostov, K. G.; Machida, M.\*; Flacker, A.

An experimental investigation comparing the properties of plasma jets in dielectric barrier discharge (DBD) configurations using a powered electrode with and without a dielectric barrier, while keeping a second dielectric barrier over the grounded electrode, is reported in this work. For this purpose, two different power sources were used to produce the plasma jets, with one of them producing a pulsed high-voltage (HV) output and the other one producing a damped sine-wave HV output, which acts as a pulse-like power source. Measurements of plasma parameters were performed for both configurations using argon and helium as working gases.

As a result, if the pulsed power source is used, significant differences were found in discharge power (P-dis) and rotational and vibrational temperatures (T-r and T-v, respectively) when switching from one configuration to the other. On the other hand, using the pulse-like HV, only the P-dis parameter presented significant differences when switching the electrode's configuration. For the pulsed source, it has been observed that despite the remarkable increase in Pdis when changing from the double barrier configuration to the single barrier one, the values obtained for T-r and T-v also increased, but not in the same proportion as the increase in P-dis, which suggests a nonlinear dependence between temperatures and discharge power in the plasma jet. As an example for application of plasmas in both configurations, tests in an attempt to remove copper films deposited on alumina substrates were performed and, as a result, there was significant material removal only when the powered electrode was in contact with the plasma. As a general conclusion, if higher power is really required for applications that do not involve in vivo targets, it is better to use this configuration.

IEEE TRANSACTIONS ON PLASMA SCIENCE 49[4], 1293-1301, 2021. DOI: 10.1109/TPS.2021.3067159

[P109-2021] "Prospects for beyond the Standard Model physics searches at the Deep Underground Neutrino Experiment DUNE Collaboration"

Abi, B.; Acciarri, R.; Acero, M. A.; Holanda, P. C. de\*; Gelli, B.\*; Guzzo, M. M.\*; Kemp, E.\*; Machado, A. A.\*; Peres, O. L. G.\*; Prakash, S.\*; Reggiani-Guzzo, M.\*; Segreto, E.\*; Nunes, M. S.\*; Forero, D. V.\*; Souza, H. V. de\*; et.al.

The Deep Underground Neutrino Experiment (DUNE) will be a powerful tool for a variety of physics topics. The high-intensity proton beams provide a large neutrino flux, sampled by a near detector system consisting of a combination of capable precision detectors, and by the massive far detector system located deep underground. This configuration sets up DUNE as a machine for discovery, as it enables opportunities not only to perform precision neutrino measurements that may uncover deviations from the present three-flavor mixing paradigm, but also to discover new particles and unveil new interactions and symmetries beyond those predicted in the Standard Model (SM). Of the many potential beyond the Standard Model (BSM) topics DUNE will probe, this paper presents a selection of studies quantifying DUNE's sensitivities to sterile neutrino mixing, heavy neutral leptons, non-standard interactions, CPT symmetry violation, Lorentz invariance violation, neutrino trident production, dark matter from both beam induced and cosmogenic sources, baryon number violation, and other new physics topics that complement those at high--energy colliders and significantly extend the present reach.

**EUROPEAN PHYSICAL JOURNAL C 81[4], 322, 2021. DOI:** 10.1140/epjc/s10052-021-09007-w

[P110-2021] "Role of Group V Atoms during GaAs Nanowire Growth Revealed by Molecular Dynamics Simulations: Implications in the Formation of Sharp Interfaces"

Oliveira, D. S.; Cotta, M. A.\*

Understanding atomistic mechanisms for catalyst-assisted nanowire growth is an essential step to improve control over the properties of these versatile nanomaterials. However, in silico approaches for III-V nanowire growth have been hindered so far mainly by the limited number of interatomic potentials. Here, we present an original interatomic potential for molecular dynamics simulations of Au-catalyzed GaAs nanowire growth.

Our simulations provide important insights about the atomic distribution in the nanowire catalyst and the role of As atoms during GaAs nanowire growth. We show that a stable, thin layer of As around the catalyst is essential for nanowire growth and that the composition of the region close to the solid-liquid interface is nonuniform, alternating between Garich and As/Au-rich layers. These features contribute to the reservoir effect, enlarging interface widths when exchanging group III or V species for heterostructure growth. Our simulation results also provide directions for challenging in situ experiments to further probe the existence of this thin As layer on the catalyst surface, as well as for finding improved conditions to obtain sharp interfaces in nanowires with axial heterostructures.

ACS APPLIED NANO MATERIALS 4[3], 2903-2909, 2021. DOI: 10.1021/acsanm.1c00057

[P111-2021] "Rolled-Up Quantum Wells Composed of Nanolayered InGaAs/GaAs Heterostructures as Optical Materials for Quantum Information Technology"

Rodrigues, L. N.; Scolfaro, D.\*; Conceicao, L. da\*; Malachias, A.; Couto, O. D. D.\*; Iikawa, F.\*; Deneke, C.\*

Strain-based band structure engineering is a powerful tool to tune the optical and electronic properties of semiconductor nanostructures. We show that we can tune the band structure of InGaAs semiconductor quantum wells and modify the helicity of the emitted light by integrating them into rolled-up heterostructures and changing their geometrical configuration. Experimental results from photoluminescence and photoluminescence excitation spectroscopy demonstrate a strong energy shift of the valence-band states in comparison to flat structures, as a consequence of an inversion of the heavy-hole with the light-hole states in a rolled-up InGaAs quantum well. The inversion and mixing of the band states lead to a strong change in the optical selection rules for the rolled-up quantum wells, which show vanishing spin polarization in the conduction band even under near-resonant excitation conditions. Band structure calculations are carried out to understand the changes in the electronic transitions and to predict the emission and absorption spectra for a given geometrical configuration. Comparison between experiment and theory shows an excellent agreement. These observed profound changes in the fundamental properties can be applied as a strategic route to develop novel optical devices for quantum information technology.

ACS APPLIED NANO MATERIALS 4[3], 3140-3147, 2021. DOI: 10.1021/acsanm.1c00354

[P112-2021] "Search for nonresonant Higgs boson pair production in final states with two bottom quarks and two photons in proton-proton collisions at root s=13 TeV"

Sirunyan, A. M.; Tumasyan, A.; Adam, W.; Chinellato, J. A.\*; Tonelli Manganote, E. J.\*; et al.; CMS Collaboration

A search for nonresonant production of Higgs boson pairs via gluon-gluon and vector boson fusion processes in final states with two bottom quarks and two photons is presented. The search uses data from proton-proton collisions at a center-of-mass energy of root s = 13 TeV recorded with the CMS detector at the LHC, corresponding to an integrated luminosity of 137 fb(-1). No significant deviation from the background-only hypothesis is observed. An upper limit at 95% confidence level is set on the product of the Higgs boson pair production cross section and branching fraction into gamma gamma b (b) over bar. The observed (expected) upper limit is determined to be 0.67 (0.45) fb, which corresponds to 7.7 (5.2) times the standard model prediction. This search has the highest sensitivity to Higgs boson pair production to date.

Assuming all other Higgs boson couplings are equal to their values in the standard model, the observed coupling modifiers of the trilinear Higgs boson self-coupling kappa(lambda) and the coupling between a pair of Higgs bosons and a pair of vector bosons c(2V) are constrained within the ranges -3.3 < kappa(lambda) < 8.5 and -1.3 < c(2V) < 3.5 at 95% confidence level. Constraints on kappa(lambda) are also set by combining this analysis with a search for single Higgs bosons decaying to two photons, produced in association with top quark-antiquark pairs, and by performing a simultaneous fit of kappa(lambda) and the top quark Yukawa coupling modifier kappa(t).

JOURNAL OF HIGH ENERGY PHYSICS 3, 257, 2021. DOI: 10.1007/JHEP03(2021)257

[P113-2021] "Search for supersymmetry in final states with two oppositely charged same-flavor leptons and missing transverse momentum in proton-proton collisions at root s=13 TeV"

Sirunyan, A. M.; Tumasyan, A.; Adam, W.; Chinellato, J. A.\*; Tonelli Manganote, E. J.\*; et al.; CMS Collaboration

A search for phenomena beyond the standard model in final states with two oppositely charged same-flavor leptons and missing transverse momentum is presented. The search uses a data sample of proton-proton collisions at root s = 13 TeV, corresponding to an integrated luminosity of 137 fb(-1), collected by the CMS experiment at the LHC. Three potential signatures of physics beyond the standard model are explored: an excess of events with a lepton pair, whose invariant mass is consistent with the Z boson mass; a kinematic edge in the invariant mass distribution of the lepton pair; and the nonresonant production of two leptons. The observed event yields are consistent with those expected from standard model backgrounds. The results of the first search allow the exclusion of gluino masses up to 1870 GeV, as well as chargino (neutralino) masses up to 750 (800) GeV, while those of the searches for the other two signatures allow the exclusion of light-flavor (bottom) squark masses up to 1800 (1600) GeV and slepton masses up to 700 GeV, respectively, at 95% confidence level within certain supersymmetry scenarios.

JOURNAL OF HIGH ENERGY PHYSICS 4, 123, 2021. DOI: 10.1007/JHEP04(2021)123

[P114-2021] "Size distribution and interaction effects on dispersed Fe30Ni70 nanoalloy synthesized by thermal decomposition"

Peixoto, E. B.; Carvalho, M. H.; Duque, J. G. S.; Muraca, D.\*; Xing, Y. T.; Nunes, W. C.

Magnetic properties of Fe30Ni70 nanoalloys dispersed in a silica matrix are reported. X-ray diffraction patterns and TEM images are consistent with a fcc crystalline structure (space group Fm3m). Thermogravimetric data and its derivative reveal important features about the kinetics formation of the nanoalloy. Magnetization data as a function of an applied magnetic field and temperature indicate that nanoalloys are superparamagnetic with blocking effects appearing around T = 10 K. However, the unusual magnetic-field-dependence of the blocking temperature suggests that interaction effects must be taken into account. In this sense, as the power law usually employed to describe noninteracting particles system do not fit our experimental data, we have used a simple modification of the random anisotropy model (RAM). Finally, once the size distribution of nanoparticles should also play a crucial role in determining the magnetic behavior of the sample, we have analyzed the T-dependence of coercive field using a generalized model, which takes into account this parameter.

JOURNAL OF MAGNETISM AND MAGNETIC MATERIALS 518, 2021. DOI: 10.1016/j.jmmm.2020.16739

[P115-2021] "Structural and morphological characterization of Ti6Al4V alloy surface functionalization based on Nb2O5 thin film for biomedical applications"

Bino, M. C. de A.; Euridice, W. A.; Gelamo, R. V.; Leite, N. B.; Silva, M. V. da; Siervo, A. de\*; Pinto, M. R.; Buranello, P. A. de A.; Moreto, J. A.

This paper proposes an applied and innovative research for the development of Nb2O5 thin film on the Ti6Al4V allov surface with great prospects of being used in the biomedical area. Thin films of Nb205 have been deposited on the Ti6Al4V alloy surface by using the reactive sputtering technique. The system was characterized morphologically and structurally via SEM/EDX, AFM, FTIR, Raman spectroscopy and XPS. Interfacial tension theory was used for the determination of the surface free energy and showed that the treated surface became more hydrophilic when compared to the bare material. The high-resolution X-ray photoelectron spectra from Nb 3d and O 1s core-levels demonstrate unequivocally the presence of a single-phase Nb2O5. Cytotoxicity and biocompatibility (VERO--CCL-81 cell line) tests as well as analyzes of inflammatory responses with Human blood leukocyte cells were also performed by showing that Nb2O5 coating reduced both Ti6Al4V alloy toxicity and its inflammation induction besides increasing the anti-inflammatory cytokine levels. Since the surface functionalization resulted in both higher biocompatibility and tolerance by immune cells besides low inflammatory levels concerning the base material, we present a superior material with wide spectra of usage in the biomedical area.

**APPLIED SURFACE SCIENCE 557, 149739, 2021. DOI:** 10.1016/j.apsusc.2021.149739

[P116-2021] "Sub-diffractional cavity modes of terahertz hyperbolic phonon polaritons in tin oxide"

Feres, F. H\*; Mayer, R. A.\*; Wehmeier, L.; Maia, F. C. B.; Viana, E. R.; Malachias, A.; Bechtel, H. A.; Klopf, J. M.; Eng, L. M.; Kehr, S. C.; Gonzalez, J. C.; Freitas, R. O.; Barcelos, I. D.

Hyperbolic phonon polaritons have recently attracted considerable attention in nanophotonics mostly due to their intrinsic strong electromagnetic field confinement, ultraslow polariton group velocities, and long lifetimes. Here we introduce tin oxide (SnO2) nanobelts as a photonic platform for the transport of surface and volume phonon polaritons in the mid- to far--infrared frequency range. This report brings a comprehensive description of the polaritonic properties of SnO2 as a nanometer-sized dielectric and also as an engineered material in the form of a waveguide. By combining accelerator-based IR-THz sources (synchrotron and free-electron laser) with s--SNOM, we employed nanoscale far-infrared hyper-spectral--imaging to uncover a Fabry-Perot cavity mechanism in SnO2 nanobelts via direct detection of phonon-polariton standing waves. Our experimental findings are accurately supported by notable convergence between theory and numerical simulations. Thus, the SnO2 is confirmed as a natural hyperbolic material with unique photonic properties essential for future applications involving subdiffractional light traffic and detection in the far-infrared range. Systems that help to enable nanophotonics in the terahertz region are in demand for developing technologies. The authors introduce and study the photonic properties of tin oxide nanobelts as such a platform, supporting phonon polaritons in the far-IR range.

NATURE COMMUNICATIONS 12[1], 1995, 2021. DOI: 10.1038/s41467-021-22209-w

[P117-2021] "The molecular structure of the surface of water-ethanol mixtures"

Kirschner, J.; Gomes, A. H. A.\*; Marinho, R. R. T.; Bjorneholm, O.; Agren, H.; Carravetta, V.; Ottosson, N.; Brito, A. N. de\*; Bakker, H. J.

Mixtures of water and alcohol exhibit an excess surface concentration of alcohol as a result of the amphiphilic nature of the alcohol molecule, which has important consequences for the physico-chemical properties of water-alcohol mixtures. Here we use a combination of intensity vibrational sum-frequency generation (VSFG) spectroscopy, heterodyne-detected VSFG (HD-VSFG), and core-level photoelectron spectroscopy (PES) to investigate the molecular properties of water-ethanol mixtures at the air-liquid interface. We find that increasing the ethanol concentration up to a molar fraction (MF) of 0.1 leads to a steep increase of the surface density of the ethanol molecules, and an increased ordering of the ethanol molecules at the surface. When the ethanol concentration is further increased, the surface density of ethanol remains more or less constant, while the orientation of the ethanol molecules becomes increasingly disordered. The used techniques of PES and VSFG provide complementary information on the density and orientation of ethanol molecules at the surface of water, thus providing new information on the molecular-scale properties of the surface of water-alcohol mixtures over a wide range of compositions. This information is invaluable in understanding the chemical and physical properties of water-alcohol mixtures.

PHYSICAL CHEMISTRY CHEMICAL PHYSICS, 2021. DOI: 10.1039/d0cp06387h

[P118-2021] "Theory of neutrino detection: flavor oscillations and weak values"

Porto-Silva, Y. P.\*; Oliveira, M. C. de\*

We revisit the theory of neutrino oscillations and describe it through the formalism of weak measurements with postselection. It is well understood that due to the large momentum uncertainty in detection, there is no collapse of the neutrino wavefunction in the momentum or energy basis, and the mass eigenstates are detected coherently. Here we show that post-selection, which projects the system to a final flavor state, deforms the system wavefunction in such a way that the momentum detected is not the expectation value of the neutrino mass eigenstates momenta, but the corresponding weak value. We use the weak values to describe the intermediate state in the oscillation process, avoiding problems in defining probability currents for particle states with mass superposition.

**EUROPEAN PHYSICAL JOURNAL C 81[4], 330, 2021. DOI:** 10.1140/epjc/s10052-021-09108-6

[P119-2021] "Toward Engineering Intrinsic Line Widths and Line Broadening in Perovskite Nanoplatelets"

Liu, A.; Nagamine, G.\*; Bonato, L. G.; Almeida, D. B.\*; Zagonel, L. F.\*; Nogueira, A. F.; Padilha, L. A.\*; Cundiff, S. T.

Perovskite nanoplatelets possess extremely narrow absorption and emission line widths, which are crucial characteristics for many optical applications. However, their underlying intrinsic and extrinsic line-broadening mechanisms are poorly understood. Here, we apply multidimensional coherent spectroscopy to determine the homogeneous line broadening of colloidal perovskite nanoplatelet ensembles. We demonstrate a dependence of not only their intrinsic line widths but also of various broadening mechanisms on platelet geometry. We find that decreasing nanoplatelet thickness by a single monolayer results in a 2-fold reduction of the inhomogeneous line width and a 3-fold reduction of the intrinsic homogeneous line width to the sub-millielectronvolts regime.

In addition, our measurements suggest homogeneously broadened exciton resonances in two-layer (but not necessarily three-layer) nanoplatelets at room-temperature.

ACS NANO 15[4], 6499-6506, 2021. DOI: 10.1021/acsnano.0c09244

[P120-2021] "Tuning the magnetic properties of Sn1-x--yCe4+xCe3+yO2 nanoparticles: an experimental and theoretical approach"

Aragon, F. F. H.; Villegas-Lelovsky, L.; Cabral, L.\*; Lima, M. P.; Mesquita, A.; Coaquira, J. A. H.

During the last decade, there was a substantial increase in the research on metal-doped oxide semiconductor nanoparticles due to advances in the engineering of nanomaterials and their potential application in spintronics, biomedicine and photocatalysis fields. In this regard, doping a nanomaterial is a powerful tool to tune its physicochemical properties. The aim of this work is to shine a new light on the role of the neighbouring elements on the oxidation state of the Ce-impurity, from both experimental and theoretical points of view. Herein, we present an accurate study of the mechanisms involved in the oxidation states of the Ce-ions during the doping process of SnO2 nanoparticles (NPs) prepared by the polymeric precursor method. X-ray diffraction measurements have displayed the tetragonal rutile-type SnO2 phase in all samples. However, the Bragg's peak (111) and (220) located at 2 theta similar to 29 degrees and similar to 47 degrees evidence the formation of a secondary CeO2 phase for samples with Ce content up to 10%. X-ray absorption near-edge structure (XANES) measurements, at Ce L3 edge, were performed on the NPs as a function of Ce content. The results show, on one side, the coexistence of Ce3+ and Ce4+ states in all samples; and on the other side, a clear reduction in the Ce3+ population driven by the increase of Ce content. It is shown that this is induced by the neighboring cation, and confirmed by magnetic measurements. The monotonic damping of the Ce3+/Ce4+ ratio experimentally, was connected with theoretical calculations via density functional theory by simulating a variety of point defects composed of Ce impurities and surrounding oxygen vacancies. We found that the number of oxygen vacancies around the Ce-ions is the main ingredient to change the Ce oxidation state, and hence the magnetic properties of Ce-doped SnO2 NPs. The presented results pave the way for handling the magnetic properties of oxides through the control of the oxidation state of impurities.

NANOSCALE ADVANCES 3[5], 1484-1495, 2021. DOI: 10.1039/d0na00700e

[P121-2021] "Tuning the shape, size, phase composition and stoichiometry of iron oxide nanoparticles: The role of phosphate anions"

Niraula, G.; Coaquira, J. A. H.; Aragon, F. H.; Villar, B. M. G.; Mello, A.; Garcia, F.; Muraca, D.\*; Zoppellaro, G.; Vargas, J. M.; Sharma, S. K.

This work describes a microwave synthetic approach for the controlled assembly of alpha-Fe2O3 nanosystems with defined morphologies, such as hollow nanotubes (NTs), solid nanorods (NRs) and nanodisks (NDs). The morphological control is aided during the crystallization processes by using phosphate anions as key surfactants in solution. Furthermore, the thermal reduction under H-2 atmosphere of these NTs, NRs and NDs alpha-Fe2O3 systems to the correspondent Fe3O4 nanomaterials preserved their initial morphologies. It was observed that the concentration of phosphate anions and volume of solvent had significant impact not only on controlling the shapes and sizes, but also phase composition and stoichiometry of the NTs, NRs and NDs nanoparticles.

X-ray Rietveld refinement analysis of the NTs, NRs and NDs systems, after reduction in H-2, revealed the presence of zero-valent iron (Fe-0) in the final materials, with Fe-0 fractions that decreased gradually in % from NTs (similar to 16%), NRs (similar to 11%) to NDs (similar to 0%) upon increasing amount of phosphate anions. Bulk magnetic susceptibility measurements showed clear alterations of the Verwey transition temperatures (T-V) and the development of unusual magnetic phenomena, such as magnetic vortex states in NDs, which was subsequently verified by micro-magnetic simulations. From the combination of XRD analysis, bulk magnetic susceptibility and M ossbauer results, we provide herein a detailed mechanistic description of the chemical processes that gated the development of shape-controlled synthesis of NTs, NRs and NDs and give a detailed correlation between specific morphology and magneto-electronic behaviors.

JOURNAL OF ALLOYS AND COMPOUNDS 856, 156940, 2021. DOI: 10.1016/j.jallcom.2020.156940

[P122-2021] "Two-dimensional MoS2-based impedimetric electronic tongue for the discrimination of endocrine disrupting chemicals using machine learning"

Christinelli, W. A.; Shimizu, F. M.\*; Facure, M. H. M.; Cerri, R.; Oliveira Junior, O. N.; Correa, D. S.; Mattoso, L. H. C.

In this paper, we report on machine learning to analyze the capacitance spectra obtained with an electronic tongue (e--tongue) and discriminate three endocrine-disrupting chemicals (EDC): bisphenol A, estrone, and 17-beta-estradiol, and their mixtures. The e-tongue comprised seven sensing units made with interdigitated gold electrodes coated with layer--by-layer films of poly(o-methoxy aniline), poly(3-thiophene acetic acid), and molybdenum disulfide (MoS2). The Multilayer Perceptron (MLP), Random Forest, and Extreme Gradient Boosting (XGBoost) models were applied for multi-target regression to predict the concentration of individual contaminants and their mixtures. These machine learning models were evaluated according to the root mean square error (RMSE) values. The best performance was achieved with XGBoost for which RMSE ranged from 0.19 to 3.37 for individual contaminants, from 0.12 to 0.25 for the mixtures, and from 0.34 to 3.46 for the entire dataset. The high performance was only possible with a multi-target regression strategy, including a feature selection procedure. In the latter, the data were plotted with the parallel coordinate technique, and the silhouette coefficient was calculated, which is a quantitative measure of the ability to distinguish similar samples in a dataset. The usefulness of the machine learning methods is demonstrated by noting that the data from mixtures of EDCs could not be distinguished using multidimensional projections. Also significant is that this combination of machine learning and information visualization methodology is entirely generic; it may be applied to analyze data from etongues and other sensing and biosensing devices in prediction tasks as demanding as in the discrimination of mixtures of EDCs at concentrations below nmol L-1.

SENSORS AND ACTUATORS B-CHEMICAL 336, 129696, 2021. DOI: 10.1016/j.snb.2021.129696

## Correções

[C006-2021] "Search for dark matter produced in association with avleptonically decaying Z boson in proton-proton collisions at root s = 13 TeV (vol 81, 13, 2021)"

Sirunyan, A. M.; Tumasyan, A.; Adam, W.; Chinellato, J. A.\*; Tonelli Manganote, E. J.\*; et al.; CMS Collaboration

EUROPEAN PHYSICAL JOURNAL C 81[4], 333, 2021. DOI: 10.1140/epjc/s10052-021-08959-3

\*Autores da comunidade IFGW Fonte: Web of Science on-line (WOS)

Defesas de Dissertações do IFGW

[D009-2021] "Descrevendo a relação entre galáxias e matéria escura em "pequenas" escalas: um estudo de modelos de ocupação de halos usando Processos Gaussianos e Otimização Bayesiana"

Aluno: Pedro Rangel Caetano

Orientador: Profa. Dra. Flavia Sobreira

Data: 26/05/2021

[D010-2021] "O vértice ghost-glúon na configuração soft-

-glúon"

Aluno: Cleiton de Oliveira Ambrósio

Orientador: Profa. Dra. Arlene Cristina Aguilar

Data: 16/06/2021

[D011-2021] "Crescimento de Cristais e Nanofios de Silício Altamente dopados com Gálio via Nanonucleação por

Fluxo Metálico"

Aluno: Raul Back Campanelli Orientador: Profa. Dra. Fanny Béron

Data: 07/07/2021

Defesas de Teses do IFGW

[T004-2021] "Estruturas de Mn-Si monocristalinas de alta qualidade para aplicações em spintrônica e nanoeletrônica"

Aluno: Alexsandro dos Santos Evangelista da Cruz

Orientador: Profa. Dra. Fanny Béron

Data: 10/05/2021

[T005-2021] "Ganho Óptico em Nanocristais Colodais"

Aluno: Gabriel Nagamine

Orientador: Prof. Dr. Lázaro Aurélio Padilha

Data: 17/05/2021

[T006-2021] "Fenomenologia de Neutrinos em Experi-

mentos de Short-Baseline" Aluno: Gabriela Vitti Stenico

Orientador: Prof. Dr. Orlando Luis Goulart Peres

Data: 24/05/2021

[T007-2021] "Acoplamento Hiperfino como sonda de hibridização em Sistemas de Elétrons Fortememnte Correlacionados"

Aluno: Paulo Eduardo Menegasso Filho

Orientador: Prof. Dr. Ricardo Rodrigues Urbano

Data: 09/06/2021

Fonte: Portal IFGW/Pós-graduação - Agenda de Colóquios,

Defesas e Seminários.

**Disponível em:** http://portal.ifi.unicamp.br/pos-graduacao

Defesas de Teses e Dissertações do PECIM

**Observação:** Não ocorreram neste período defesas de teses e dissertações, com orientadores ou banca do IFGW, do Programa de Pós-Graduação Multiunidades em Ensino de Ciências e Matemática - Mestrado e Doutorado (PECIM) da Unicamp.

Fonte: Página do PECIM

Disponível em: https://www.pecim.unicamp.br/bancas

## **Abstracta**

Instituto de Física

Diretor: Prof. Dr. Pascoal José Giglio Pagliuso Diretora Associada: Profa. Dra. Mônica Alonso

Cotta

Universidade Estadual de Campinas - UNICAMP

Cidade Universitária Zeferino Vaz 13083-859 - Campinas - SP - Brasil e-mail: secdir@ifi.unicamp.br

Fone: +55 19 3521-5300

**Publicação** 

Biblioteca do Instituto de Física Gleb Wataghin http://portal.ifi.unicamp.br/biblioteca

Diretora Técnica: Sandra Maria Carlos Cartaxo Coordenadora da Comissão de Biblioteca: Profa. Dra. Arlene Cristina Aguilar

Elaboração:

Maria Graciele Trevisan (Bibliotecária)

Ayres Neri da Cunha Junior (Técnico Administrativo)

contato: infobif@ifi.unicamp.br